A Neumann series based method for photoacoustic tomography on irregular domains

Eric Chung, Chi Yeung Lam, and Jianliang Qian

Abstract. Recently, a Neumann series based numerical method is developed for photoacoustic tomography in a paper by Qian, Stefanov, Uhlmann, and Zhao [*An efficient neumann series-based algorithm for thermoacoustic and photoacoustic tomography with variable sound speed.* SIAM J. Imag. Sci., 4:850–883, 2011]. It is an efficient and convergent numerical scheme that recovers the initial condition of an acoustic wave equation with non-constant sound speeds by boundary measurements. In practical applications, the domains of interest typically have irregular geometries and contain media with discontinuous sound speeds, and these issues pose challenges for the development of efficient solvers. In this paper, we propose a new algorithm which is based on the use of the staggered discontinuous Galerkin method for solving the underlying wave propagation problem. It gives a convenient way to handle domains with complex geometries and discontinuous sound speeds. Our numerical results show that the method is able to recover the initial condition accurately.

1. Introduction

Mathematical imaging is an important research field in applied mathematics. There have been many significant progresses in both mathematical theories and medical applications; see [**7, 9, 8, 10, 3, 1, 12, 13, 14, 15, 16, 17, 19, 20, 22, 23, 25, 26, 29, 31, 32, 18**] and references therein. Theoretically, one is interested in uniqueness and stability of the solution for the inverse problem; numerically, one is interested in designing efficient numerical algorithms to recover the solution of the inverse problem. Naturally, the above two aspects have been well studied in the case of the sound speed being constant. In fact, if the sound speed is constant and the observation surface $\partial\Omega$ is of some special geometry, such as planar, spherical or cylindrical surface, there are explicit closed-form inversion formulas; see [**12, 28, 14, 15, 11**] and references therein. In practice the constant sound speed model is inaccurate in many situations [**29, 18, 30, 21**]. For instance in breast imaging, the different components of the breast, such as the glandular tissues, stromal tissues, cancerous tissues and other fatty issues, have different acoustic properties. The variations between their acoustic speeds can be as great as 10% [**18**].

The research of Eric Chung is partially supported by the CUHK Focused Investment Scheme 2012-14. The research of Jianliang Qian is partially supported by NSF..

In this paper, we will focus on photoacoustic tomography which is a very important field in mathematical imaging. Photoacoustic tomography has recently attracted much attention due to its applications in medical imaging. It is based on the non-destructive testing methodology to construct high resolution medical images needed for important diagnostic processes. The physical mechanism involved is the so-called photoacoustic effect, which can be briefly described as follows. Initially, a short pulse of electromagnetic wave is injected into the patient's body. Then the body is heated up which generates some acoustic waves. Different parts of the body have different absorption rates, and this information is contained in the acoustic waves generated by this process. The body structure is then determined by measuring the acoustic waves outside of the patient's body. For more details about this, see for example [**29, 27**].

Now, we will present the mathematical formulation of photoacoustic tomography. Let $\Omega \subset \mathbb{R}^n$ be an open set having smooth and strictly convex boundary $\partial\Omega$. This domain Ω is understood as the body of interest. As mentioned previously, a pulse of electromagnetic signals will generate some heat and then acoustic waves, the heating process is modeled by the initial condition of the wave propagation problem. More precisely, given a source function $f(x)$ with support in $\overline{\Omega}$ initially, it will generate acoustic signals. The photoacoustic tomography problem is to determine the unknown source function $f(x)$ by boundary measurements of these acoustic signals. The forward problem can be described as follows. Given the initial condition $f(x)$, the acoustic pressure $u(t,x)$ satisfies

$$\frac{\partial^2 u}{\partial t^2} - c^2 \Delta u = 0, \quad \text{in} \quad (0,T) \times \mathbb{R}^n \tag{1}$$

subject to the following initial conditions

$$u(0,x) = f(x), \qquad u_t(0,x) = 0, \qquad \text{on} \quad \mathbb{R}^n. \tag{2}$$

In the above wave equation (1), the function $c(x)$ is the acoustic sound speed. We assume that $c(x)$ is a given, possibly discontinuous, function inside Ω and takes the value one outside Ω. Our measurement can be represented by an operator Λ defined by

$$\Lambda f := u\big|_{[0,T]\times\partial\Omega} \tag{3}$$

which is the value of the acoustic pressure $u(t,x)$ along the boundary of the domain $\partial\Omega$ for all times.

In this paper, we propose a new numerical algorithm that works for irregular domains by following [**24**]. In [**24**], the method is applied to rectangular domains; in the current work, we extend the idea to unstructured domains so that the methodology is applicable to more practical situations. To achieve our goals, we will apply the staggered discontinuous Galerkin method [**5, 6**] for the numerical approximation of the wave propagation problem. It gives a systematic way to handle domains with complicated geometries and discontinuous sound speeds. Moreover, there are distinctive advantages of using the staggered discontinuous Galerkin method; namely, the method is an explicit scheme which allows very efficient time stepping. Besides, the method is able to preserve the wave energy and gives smaller dispersion errors compared with non-staggered schemes [**4, 2**]. In addition, we also need a Poisson solver on irregular domains for our reconstruction algorithm, which will be based on an integral equation approach so that we can handle a wide class of boundary

curves. Combining the above methodologies, the resulting method is very efficient and allows us to solve problems arising from realistic imaging applications.

The paper is organized as follows. In Section 2, we will present some background materials, and in Section 3, the reconstruction method together with the implementation details will be presented. Moreover, a brief account of the staggered discontinuous Galerkin method is included. Numerical results are shown in Section 4 to demonstrate the performance of our method.

2. Background

Assume for now that $c > 0$ is smooth. The speed c defines a Riemannian metric $c^{-2}\mathrm{d}x^2$. For any piecewise smooth curve $\gamma : t \in [a, b] \mapsto \gamma(t) \in \mathbb{R}^n$, the length of γ in that metric is given by

$$\text{length}(\gamma) = \int_a^b \frac{|\dot\gamma(t)|}{c(\gamma(t))}\mathrm{d}t.$$

The so-defined length is independent of the parameterization of γ. The distance function $\text{dist}(x, y)$ is then defined as the infimum of the lengths of all such curves connecting x and y.

For any $(x, \theta) \in \mathbb{R}^n \times S^{n-1}$ we denote by $\gamma_{x,\theta}(t)$ the unit speed (i.e., $|\dot\gamma| = c(\gamma)$) geodesics issued at x in the direction θ.

Similar to the settings in [**25, 26**], the energy of $u(t, x)$ in a domain $U \subset \mathbb{R}^n$ is given by

$$E(u(t)) = \int_U \left(|\nabla_x u|^2 + c^{-2}|u_t|^2\right) \mathrm{d}x,$$

where $u(t) = u(t, \cdot)$. The energy of any Cauchy data (f, g) for equation (1) is given by

$$E(f, g) = \int_U \left(|\nabla_x f|^2 + c^{-2}|g|^2\right) \mathrm{d}x.$$

The energy norm is defined as the square root of the energy. In particular, the energy of $(f, 0)$ in U is given by the square of the Dirichlet norm

$$\|f\|^2_{H_D(U)} := \int_U |\nabla_x f|^2 \,\mathrm{d}x,$$

where the Hilbert space $H_D(U)$ is the completion of $C_0^\infty(U)$ under the above Dirichlet norm. We always assume below that the initial condition $f \in H_D(\Omega)$. We will denote by $\|\cdot\|$ the norm in $H_D(\Omega)$, and in the same way we denote the operator norm in that space.

There are two main geometric quantities that are crucial for the results below. First we set

$$T_0 := \max\{\text{dist}(x, \partial\Omega) :\ x \in \bar\Omega\}, \tag{4}$$

where $\text{dist}(x, \partial\Omega)$ is the distance in the given Riemannian metric $c^{-2}\mathrm{d}x^2$. Let $T_1 \le \infty$ be the supremum of the lengths of all maximal geodesics lying in $\bar\Omega$. Clearly, $T_0 < T_1$; however, while the first number is always finite, the second one can be infinite. It can be shown actually that

$$T_0 \le T_1/2. \tag{5}$$

3. The reconstruction method

In this section, we will present the numerical reconstruction method for the photoacoustic tomography. In [**25**], it is proved that the solution can be represented by a convergent Neumann series. Our method is based on a truncation of this Neumann series, and the addition of each term provides a refinement of the recovered solution. Thus, depending on the error tolerance, typically a few terms are needed to obtain a reasonable solution.

Assume that $f(x)$ is the unknown initial condition and that the boundary data Λf defined on $\partial\Omega$ has been given. Note that Λf is the measurement we obtained. One major step of our reconstruction method is to solve a backward in time wave propagation problem by using the boundary condition Λf. Let $v(t,x)$ be the solution of this problem. To find the solution v, we will need to specify the values of v and v_t at the final time T. For v_t, we will take $u_t = 0$ at the final time T. For v, since we only know the boundary values at the final time T, we will use a function that minimizes the energy $\|\cdot\|_{H_D(\Omega)}$. Thus, we will use the harmonic extension of Λf. To better present our ideas, for a given ϕ defined on $\partial\Omega$, we define $P\phi$ to be the harmonic extension of ϕ.

We then solve the following modified back projection problem. Given a function h defined on $\partial\Omega$, we find $v(0,\cdot)$ such that

$$\frac{\partial^2 v}{\partial t^2} - c^2\Delta v = 0, \quad \text{in} \quad (0,T)\times\Omega \tag{6}$$

subject to the boundary condition

$$v(t,x) = h, \quad \text{on} \quad [0,T]\times\partial\Omega \tag{7}$$

and the final time conditions

$$v(T,x) = Ph, \quad , v_t(T,x) = 0, \qquad \text{on} \quad \Omega. \tag{8}$$

We can then define an operator $Ah = v(0,\cdot)$. Note that, the operator A is not an actual inverse of the operator Λ, but it gives some kind of approximation.

As in [**24**], we have

$$A\Lambda = I - K \tag{9}$$

where K is an error operator. Under suitable conditions, it is proved in [**25**] that

$$\|Kf\|_{H_D(\Omega)} \le \|f\|_{H_D(\Omega)} \tag{10}$$

and that

$$\|K\|_{H_D(\Omega)\to H_D(\Omega)} < 1. \tag{11}$$

Therefore, one can write the following Neumann series [**25**]

$$f = \sum_{m=0}^{\infty} K^m A\Lambda f. \tag{12}$$

This is the key of our reconstruction algorithm. We remark that it is important to choose the final time T in a suitable way. We will use the idea described in [**24**].

Now we summarize the following properties proved in [**25**], which provides some guidances in choosing the final time T.

(i) $T < T_0$.

Λf does not recover f uniquely. Then $\|K\| = 1$, and for any f supported in the inaccessible region, $Kf = f$.

(ii) $T_0 < T < T_1/2$.
This can happen only if there is a strict inequality in (5). Then we have uniqueness but not stability. In this case, $\|K\| = 1$, $\|Kf\| < \|f\|$, and we do not know if the Neumann series (12) converges. If it does, it converges to f.

(iii) $T_1/2 < T < T_1$.
This assumes that Ω is non-trapping for c. The Neumann series (12) converges exponentially but may be not as fast as in the next case. There is stability, and $\|K\| < 1$.

(iv) $T_1 < T$.
This also assumes that Ω is non-trapping for c. The Neumann series (12) converges exponentially. There is stability, $\|K\| < 1$, and K is compact.

Now, we will present some implementation details. In (12), we can evaluate the operator A by solving the modified back-projection problem defined in (6), (7) and (8). Then, for a given function ψ defined on Ω, we can evaluate K by

$$K\psi = \psi - A(\Lambda\psi). \tag{13}$$

This means that, we have to solve the forward in time wave propagation problem with initial condition ψ and then obtain the operator $\Lambda\psi$, which is the boundary values for all times. Then using this boundary function, we solve the modified back-projection problem defined in (6), (7) and (8) to obtain $A(\Lambda\psi)$.

To solve the forward in time wave equation (1) and (2), we write it as a first order form

$$\begin{aligned} \rho\frac{\partial u}{\partial t} - \nabla\cdot p &= 0 \\ \frac{\partial p}{\partial t} - \nabla u &= 0 \end{aligned} \tag{14}$$

where $\rho = c^{-2}$ and $p = \nabla u$. To solve (14) on unstructured grid, we use the staggered discontinuous Galerkin method [**5, 6, 4**], which gives an explicit and energy conserving forward solver. We remark that explicit solver gives a very fast time-marching process. Besides, the method produces smaller dispersion errors compared with non-staggered methods [**4, 2**]. Moreover, the staggered discontinuous Galerkin method can be seen as an extension to unstructured grid of the finite difference method used in [**24**]. For completeness, we will give a brief account of the method in the next subsection. Notice that the problem (14) is posed on the whole $\mathbb{R}^n$. Thus, some artificial boundary condition is needed. In this paper, the perfectly matched layer is used as the artificial boundary condition and we use $\widehat{\Omega}$ to represent the computational domain. Finally, the values of the pressure $u(t, x)$ from (14) can then be obtained on the domain boundary $\partial\Omega$.

Another step of our reconstruction method is to generate a final time condition for the problem (6), (7) and (8). To do this, we need to find the harmonic extension for a function ϕ defined on $\partial\Omega$. To perform this step in an efficient way, we will apply the standard integral equation approach, which will be briefly accounted in the next section. Once the final time conditions are known, we can then solve the modified back-projection problem (6), (7) and (8) by the staggered discontinuous Galerkin method [**5, 6, 4**] together with the given boundary data h.

3.1. The staggered discontinuous Galerkin method. In this section, we briefly summarize the method developed in [**6**]. We start with the triangulation of the domain.

Assume that the domain Ω is triangulated by a family of triangles $\mathcal{T}$ so that $\Omega = \cup\{\tau \mid \tau \in \mathcal{T}\}$. Let $\tau \in \mathcal{T}$. We define h_τ as the diameter of τ and ρ_τ as the supremum of the diameters of the circles inscribed in τ. The mesh size h is defined as $h = \max_{\tau\in\mathcal{T}} h_\tau$. We will assume that the set of triangles $\mathcal{T}$ forms a regular family of triangulation of Ω so that there exist a uniform constant K independent of the mesh size such that

$$h_\tau \leq K\rho_\tau \quad \forall \tau \in \mathcal{T}.$$

Let $\mathcal{E}$ be the set of all edges and let $\mathcal{E}^0 \subset \mathcal{E}$ be the set of all interior edges of the triangles in $\mathcal{T}$. The length of $\sigma \in \mathcal{E}$ will be denoted by h_σ. We also denote by $\mathcal{N}$ the set of all interior nodes of the triangles in $\mathcal{T}$. Here, by interior edge and interior node, we mean any edge and node that does not lie on the boundary $\partial\Omega$. Let $\nu \in \mathcal{N}$. We define

$$\mathcal{S}(\nu) = \cup\{\tau \in \mathcal{T} \mid \nu \in \tau\}. \tag{15}$$

That is, $\mathcal{S}(\nu)$ is the union of all triangles having vertex ν. We will assume that the triangulation of Ω satisfies the following condition.

Assumption on triangulation: There exists a subset $\mathcal{N}_1 \subset \mathcal{N}$ such that

(A1) $\Omega = \cup\{\mathcal{S}(\nu) \mid \nu \in \mathcal{N}_1\}$.

(A2) $\mathcal{S}(\nu_i) \cap \mathcal{S}(\nu_j) \in \mathcal{E}^0$ for all distinct $\nu_i, \nu_j \in \mathcal{N}_1$.

Let $\nu \in \mathcal{N}_1$. We define

$$\mathcal{E}_u(\nu) = \{\sigma \in \mathcal{E} \mid \nu \in \sigma\}. \tag{16}$$

That is, $\mathcal{E}_u(\nu)$ is the set of all edges that have ν as one of their endpoints. We further define

$$\mathcal{E}_u = \cup\{\mathcal{E}_u(\nu) \mid \nu \in \mathcal{N}_1\} \quad \text{and} \quad \mathcal{E}_v = \mathcal{E}\backslash\mathcal{E}_u. \tag{17}$$

Notice that $\mathcal{E}_u$ contains only interior edges since one of the endpoints of edges in $\mathcal{E}_u$ has a vertex from $\mathcal{N}_1$. On the other hand, $\mathcal{E}_v$ has both interior and boundary edges. So, we also define $\mathcal{E}_v^0 = \mathcal{E}_v \cap \mathcal{E}^0$ which contains elements from $\mathcal{E}_v$ that are interior edges. Notice that we have $\mathcal{E}_v\backslash\mathcal{E}_v^0 = \mathcal{E} \cap \partial\Omega$. Furthermore, for $\sigma \in \mathcal{E}_v^0$, we will let $\mathcal{R}(\sigma)$ be the union of the two triangles sharing the same edge σ. For $\sigma \in \mathcal{E}_v\backslash\mathcal{E}_v^0$, we will let $\mathcal{R}(\sigma)$ be the only triangle having the edge σ.

In practice, triangulations that satisfy assumptions (A1)–(A2) are not difficult to construct. In Figure 1, we illustrate how this kind of triangulation is generated. First, the domain Ω is triangulated by a family of triangles, called $\tilde{\mathcal{T}}$. Each triangle in this family is then subdivided into three sub-triangles by connecting a point inside the triangle with its three vertices. Then we define the union of all these sub-triangles to be our triangulation $\mathcal{T}$. Each triangle in $\tilde{\mathcal{T}}$ corresponds to an $\mathcal{S}(\nu)$ for some ν inside the triangle. In Figure 1, we show two of the triangles, enclosed by solid lines, in this family $\tilde{\mathcal{T}}$. This corresponds to 6 triangles in the triangulation $\mathcal{T}$. The dotted lines represent edges in the set $\mathcal{E}_u$ while solid lines represent edges in the set $\mathcal{E}_v$.

Now, we will discuss the FE spaces. Let $k \geq 0$ be a nonnegative integer. Let $\tau \in \mathcal{T}$ and $\kappa \in \mathcal{F}$. We define $P^k(\tau)$ and $P^k(\kappa)$ as the spaces of polynomials of degree less than or equal to k on τ and κ, respectively. The method is based on the following local conforming spaces.

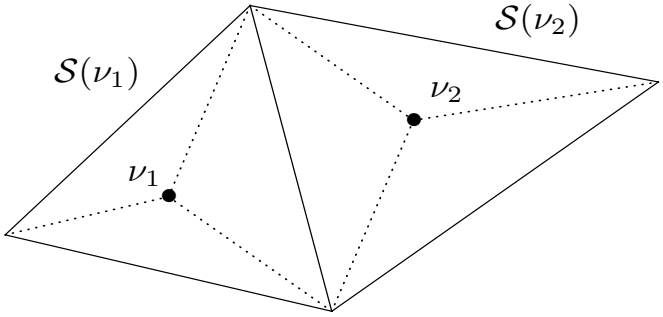

FIGURE 1. Triangulation.

Local $H^1(\Omega)$-conforming FE space:

$$U_h = \{v \mid v|_\tau \in P^k(\tau);\ v \text{ is continuous on } \kappa \in \mathcal{F}_u^0;\ v|_{\partial\Omega} = 0\}. \tag{18}$$

Notice that if $v \in U_h$, then $v|_{\mathcal{R}(\kappa)} \in H^1(\mathcal{R}(\kappa))$ for each face $\kappa \in \mathcal{F}_u$. Furthermore, the condition $v|_{\partial\Omega} = 0$ is equivalent to $v|_\kappa = 0$, $\forall \kappa \in \mathcal{F}_u \backslash \mathcal{F}_u^0$, since $\mathcal{F}_u$ contains all boundary faces. Next, we define the following space.

Local $H(\mathrm{div};\Omega)$-conforming FE space:

$$W_h = \{\mathbf{q} \mid \mathbf{q}|_\tau \in P^k(\tau)^3 \text{ and } \mathbf{q}\cdot n \text{ is continuous on } \kappa \in \mathcal{F}_p\}. \tag{19}$$

Notice that if $\mathbf{q} \in W_h$, then $\mathbf{q}|_{\mathcal{S}(\nu)} \in H(\mathrm{div};\mathcal{S}(\nu))$ for each $\nu \in \mathcal{N}_1$.

With all the above notations, the staggered discontinuous Galerkin method [**6**] is then stated as: find $u_h \in U_h$ and $\mathbf{p}_h \in W_h$ such that

$$\int_\Omega \rho \frac{\partial u_h}{\partial t}\, v\, dx + B_h(\mathbf{p}_h, v) = 0, \tag{20}$$

$$\int_\Omega \frac{\partial \mathbf{p}_h}{\partial t} \cdot \mathbf{q}\, dx - B_h^*(u_h, \mathbf{q}) = 0, \tag{21}$$

for all $v \in U_h$ and $\mathbf{q} \in W_h$, where

$$B_h(\mathbf{p}_h, v) = \int_\Omega \mathbf{p}_h \cdot \nabla v\, dx - \sum_{\kappa\in\mathcal{F}_p} \int_\kappa \mathbf{p}_h \cdot n\, [v]\, d\sigma, \tag{22}$$

$$B_h^*(u_h, \mathbf{q}) = -\int_\Omega u_h\, \nabla\cdot\mathbf{q}\, dx + \sum_{\kappa\in\mathcal{F}_u^0} \int_\kappa u_h\, [\mathbf{q}\cdot n]\, d\sigma, \tag{23}$$

where $[v]$ represents the jump of the function v. We remark that the important energy conservation property comes from the fact that $B_h(\mathbf{p}_h, u_h) = B_h^*(u_h, \mathbf{p}_h)$.

3.2. The boundary integral method. In this section, we will give a brief overview of the boundary integral method for finding the harmonic extension of ϕ defined on $\partial\Omega$. Recall that $\Omega \subset \mathbb{R}^n$ for $n \geq 2$. Let

$$K(x) = \begin{cases} \frac{1}{2\pi}\log r & n = 2 \\ \frac{1}{(2-n)\omega_n} r^{2-n} & n \geq 3 \end{cases} \tag{24}$$

where ω_n is the area of the boundary of the unit sphere in $\mathbb{R}^n$ and $r = |x|$. Then it is well known that

$$P\phi = \int_{\partial\Omega} \phi(x) \frac{\partial K(x-\xi)}{\partial \nu_x} \, d\sigma_x \tag{25}$$

where $d\sigma_x$ is the surface measure on $\partial\Omega$ and ν_x is the unit outward normal vector defined on $\partial\Omega$.

4. Numerical examples

In this section, we will present some numerical examples. We will test our numerical algorithm on some domains with irregular shapes. In all cases below, the computational domain $\widehat{\Omega}$ is $[-1.5, 1.5]^2$. Moreover, the perfectly matched layer is imposed in the region $[-1.5, 1.5]^2 \backslash [-1.05, 1.05]^2$. The mesh size for the spatial domain is taken as 0.02 and the time step size is taken according to the CFL condition which allows stability of the wave propagation solver. The final time T is taken as 4 which is large enough to guarantee the convergence of the Neumann series (12).

4.1. Example 1. In our first example, we consider the imaging of the Shepp-Logan phantom contained in the domain Ω which is a circle centered at $(0, 0)$ with radius 1. In the first test case, we take $c_1(x, y) = 1 + 0.2\sin(2\pi x) + 0.1\cos(2\pi y)$ as the sound speed inside Ω. In Figure 2, the exact solution is shown, where we see that the Shepp-Logan phantom is located inside a circular domain. Moreover, a coarse triangulation of this circular domain is also shown in Figure 2. Here, we use a coarse triangulation for display purpose, and the actual triangulation for our computation is finer than this.

The numerical reconstruction results are shown in Figure 3. From these figures, we see that the use of the first two terms in the Neumann series (12) is sufficient to give very promising results. In particular, with the use of one term in the Neumann series, we obtain a reconstruction with relative error of 4.46% while the use of two terms in the Neumann series gives a reconstruction with relative error of 2.14%.

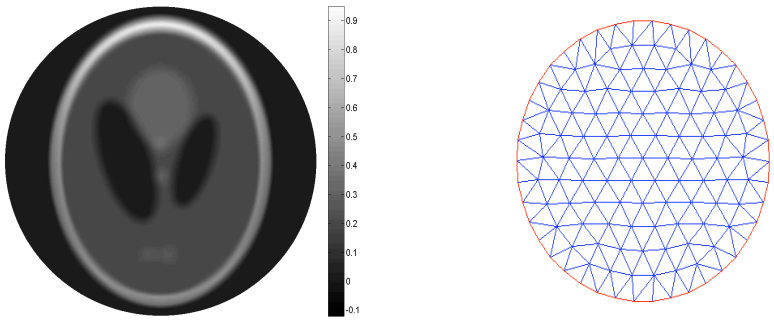

FIGURE 2. Left: exact solution. Right: an example of the mesh used for the domain.

In the second case, we take a piecewise constant sound speed $c_2(x, y)$ with the value 1.2 in the circle centered at $(0, 0)$ and radius 0.6 and the value 1.1 elsewhere

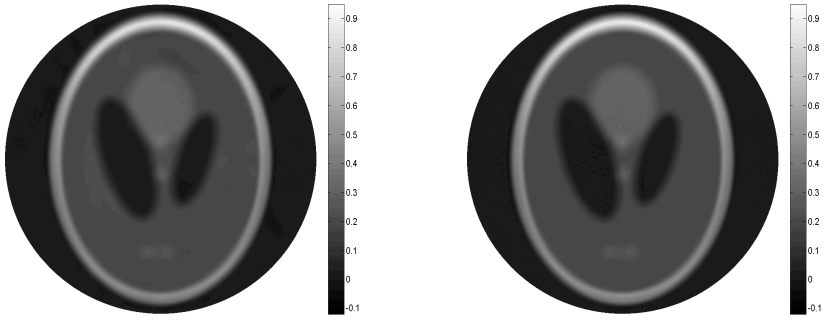

FIGURE 3. Numerical solutions. Left: one term approximation, relative error is 4.46%. Right: two term approximation, relative error is 2.14%.

in the domain Ω. The numerical reconstruction results are shown in Figure 4 while the exact solution is shown in Figure 2. From these figures, we see that the use of the first two terms in the Neumann series (12) is sufficient to give very promising results. In particular, with the use of one term in the Neumann series, we obtain a reconstruction with relative error of 2.86% while the use of two terms in the Neumann series gives a reconstruction with relative error of 2.18%.

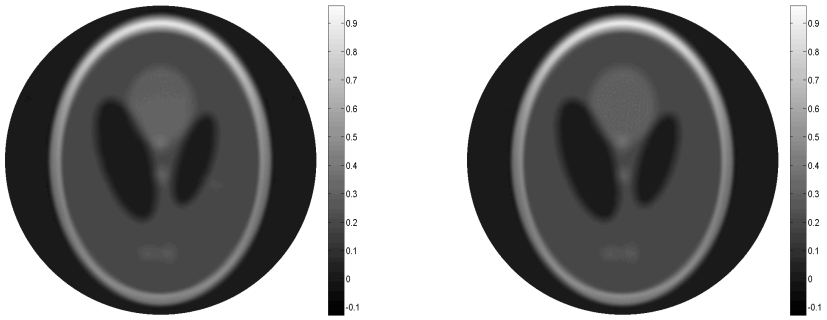

FIGURE 4. Numerical solutions. Left: one term approximation, relative error is 2.86%. Right: two term approximation, relative error is 2.18%.

For our last test case with this domain, we take the sound speed $c_2(x, y)$ defined above and add 2% noise in the data. The numerical reconstruction results are shown in Figure 5 while the exact solution is shown in Figure 2. From these figures, we see that the use of the first two terms in the Neumann series (12) is sufficient to give very promising results. In particular, with the use of one term in the Neumann series, we obtain a reconstruction with relative error of 3.18% while the use of two terms in the Neumann series gives a reconstruction with relative error of 3.10%.

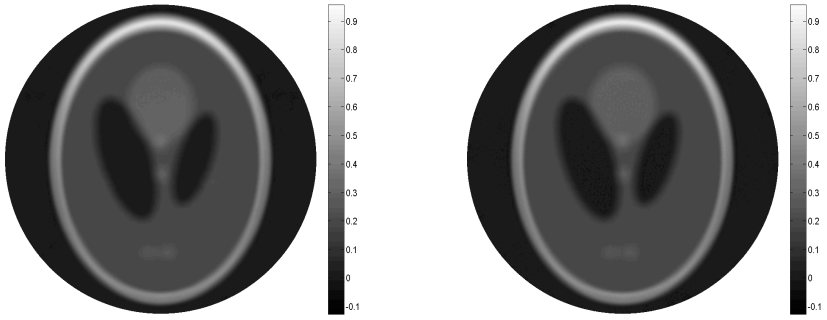

FIGURE 5. Numerical solutions. Left: one term approximation, relative error is 3.18%. Right: two term approximation, relative error is 3.10%.

4.2. Example 2. In our second example, we consider a domain with irregular shape, shown in Figure 6. Moreover, a sample triangulation of this domain is also shown in Figure 6. We use $c_1(x, y)$ as the sound speed in this test case.

We will first consider the imaging of a point source in this domain. The exact point source is shown in Figure 6. The numerical reconstruction results are shown in Figure 7. From these figures, we see that the use of the first two terms in the Neumann series (12) is sufficient to give very promising results. In particular, with the use of one term in the Neumann series, we obtain a reconstruction with relative error of 4.10% while the use of two terms in the Neumann series gives a reconstruction with relative error of 0.82%.

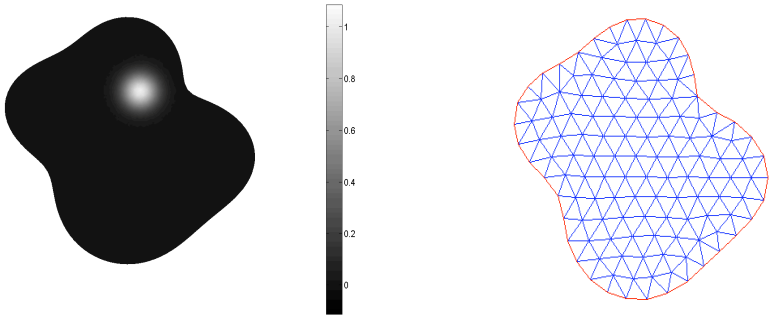

FIGURE 6. Left: exact solution. Right: an example of the mesh used for the domain.

Next, We will consider the imaging of the Shepp-Logan phantom in this domain. The exact solution is shown in Figure 8. The numerical reconstruction results are shown in Figure 9. From these figures, we see that the use of the first two terms in the Neumann series (12) is sufficient to give very promising results. In particular, with the use of one term in the Neumann series, we obtain a reconstruction with

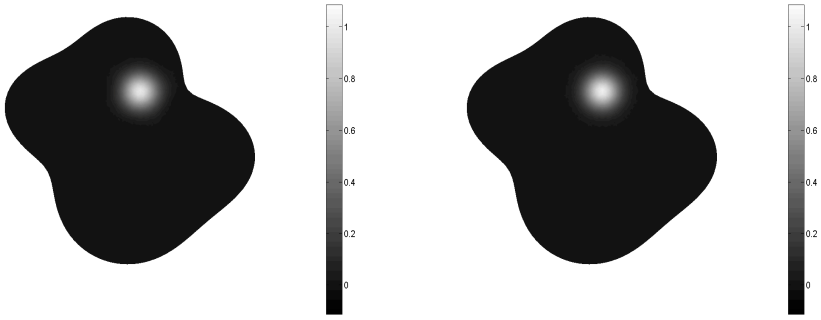

FIGURE 7. Numerical solutions. Left: one term approximation, relative error is 4.10%. Right: two term approximation, relative error is 0.82%.

relative error of 9.23% while the use of two terms in the Neumann series gives a reconstruction with relative error of 6.92%.

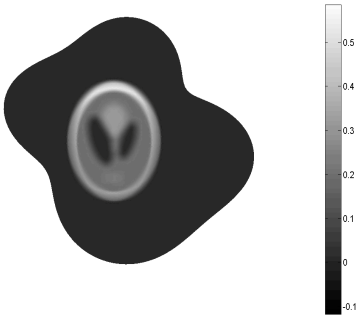

FIGURE 8. The exact solution.

4.3. Example 3. In our third example, we consider a domain with irregular shape, shown in Figure 10. Moreover, a sample triangulation of this domain is also shown in Figure 10. We use $c_1(x, y)$ as the sound speed in this test case.

We will first consider the imaging of a single Shepp-Logan phantom in this domain. The exact solution is shown in Figure 10. The numerical reconstruction results are shown in Figure 11. From these figures, we see that the use of the first two terms in the Neumann series (12) is sufficient to give very promising results. In particular, with the use of one term in the Neumann series, we obtain a reconstruction with relative error of 4.76% while the use of two terms in the Neumann series gives a reconstruction with relative error of 3.41%.

We next consider the imaging of a single Shepp-Logan phantom together with two circular objects in the domain shown in Figure 10. The exact solution is shown in Figure 12. The numerical reconstruction results are shown in Figure 13. From

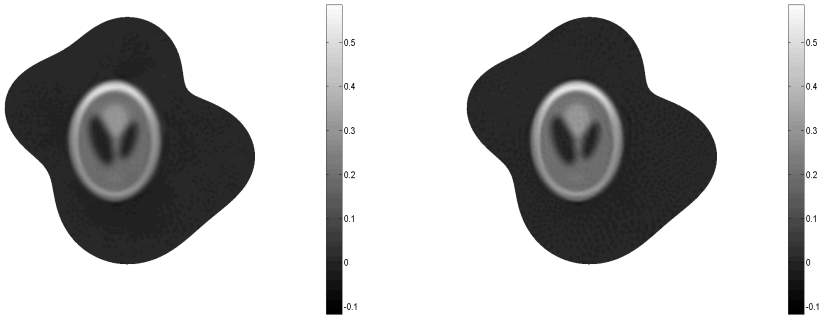

FIGURE 9. Numerical solutions. Left: one term approximation, relative error is 9.23%. Right: two term approximation, relative error is 6.92%.

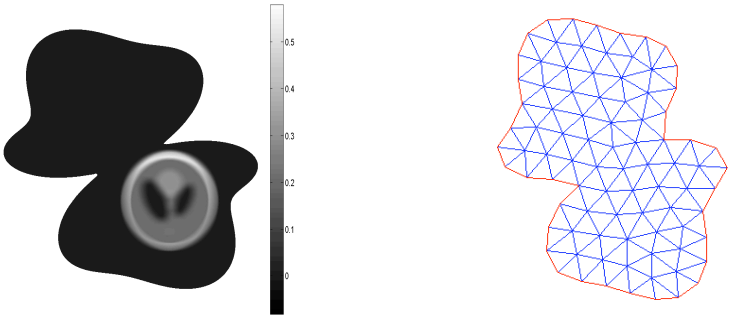

FIGURE 10. Left: exact solution. Right: an example of the mesh used for the domain.

these figures, we see that the use of the first two terms in the Neumann series (12) is sufficient to give very promising results. In particular, with the use of one term in the Neumann series, we obtain a reconstruction with relative error of 4.62% while the use of two terms in the Neumann series gives a reconstruction with relative error of 2.61%.

Next we consider the same example with 2% noise added in the data. The exact solution is shown in Figure 12. The numerical reconstruction results are shown in Figure 13. From these figures, we see that the use of the first two terms in the Neumann series (12) is sufficient to give very promising results. In particular, with the use of one term in the Neumann series, we obtain a reconstruction with relative error of 4.81% while the use of two terms in the Neumann series gives a reconstruction with relative error of 3.39%.

5. Conclusion

In this paper, we propose an efficient and accurate method for photoacoustic tomography. The method is based on a convergent Neumann series and is applicable

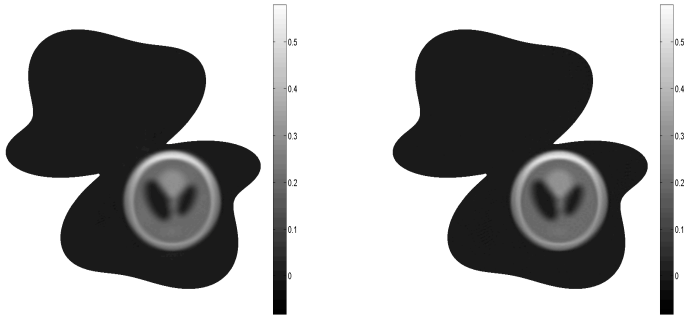

FIGURE 11. Numerical solutions. Left: one term approximation, relative error is 4.76%. Right: two term approximation, relative error is 3.41%.

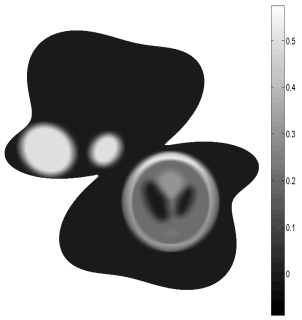

FIGURE 12. The exact solution.

to domains with complicated geometries and discontinuous sound speeds. The use of the staggered discontinuous Galerkin method allows a very efficient time-stepping and conservation of wave energy. Our numerical results show that the method has superior performance, and provides a solver for realistic imaging applications.

References

[1] M. Agranovsky, P. Kuchment, and L. Kunyansky. On reconstruction formulas and algorithms for the thermoacoustic tomography. *Photoacoustic Imaging and Spectroscopy, CRC Press*, pages 89–101, 2009.

[2] H. Chan, E. Chung, and G. Cohen. Stability and dispersion analysis of staggered discontinuous Galerkin method for wave propagation. *Int. J. Numer. Anal. Model.*, 10:233–256, 2013.

[3] E. Chung, T. F. Chan, and X. C. Tai. Electrical impedance tomography using level set representation and total variational regularization. *J. Comput. Phys.*, 205:357–372, 2005.

[4] E. Chung, P. Ciarlet, and T. Yu. Convergence and superconvergence of staggered discontinuous Galerkin methods for the three-dimensional Maxwell's equations on Cartesian grids. *J. Comput. Phys.*, 235:14–31, 2013.

[5] E. Chung and B. Engquist. Optimal discontinuous Galerkin methods for wave propagation. *SIAM J. Numer. Anal.*, 44:2131–2158, 2006.

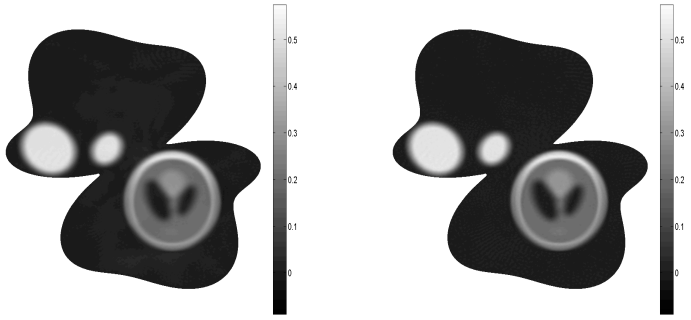

FIGURE 13. Numerical solutions. Left: one term approximation, relative error is 4.62%. Right: two term approximation, relative error is 2.61%.

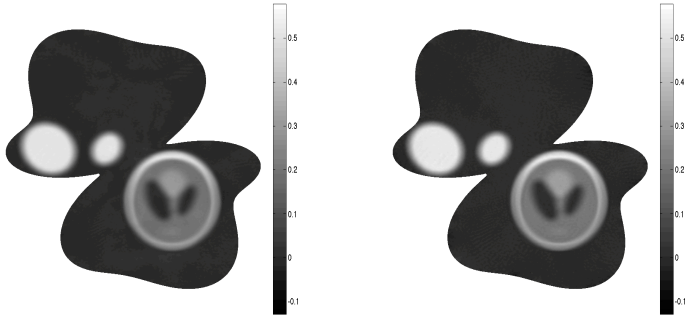

FIGURE 14. Numerical solutions. Left: one term approximation, relative error is 4.81%. Right: two term approximation, relative error is 3.39%.

[6] E. Chung and B. Engquist. Optimal discontinuous Galerkin methods for the acoustic wave equation in higher dimensions. *SIAM J. Numer. Anal.*, 47:3820–3848, 2009.
[7] E. Chung, J. Qian, G. Uhlmann, and H. Zhao. A new phase space method for recovering index of refraction from travel times. *Inverse Problems*, 23:309–329, 2007.
[8] E. Chung, J. Qian, G. Uhlmann, and H. Zhao. A phase-space formulation for elastic-wave traveltime tomography. *J. Phys.: Conf. Ser.*, 124:012018, 2008.
[9] E. Chung, J. Qian, G. Uhlmann, and H. Zhao. An adaptive phase space method with application to reflection traveltime tomography. *Inverse Problems*, 27:115002, 2011.
[10] E. Chung and J. Wong. A TV-based iterative regularization method for the solutions of thermal convection problems. *Comm. Comput. Phys.*, To appear.
[11] D. Finch, M. Haltmeier, and Rakesh. Inversion of spherical means and the wave equation in even dimensions. *SIAM J. Appl. Math.*, 68:392–412, 2007.
[12] D. Finch, S. K. Patch, and Rakesh. Determining a function from its mean values over a family of spheres. *SIAM J. Math. Anal.*, 35(5):1213–1240 (electronic), 2004.
[13] D. Finch and Rakesh. Recovering a function from its spherical mean values in two and three dimensions. *in: Photoacoustic Imaging and Spectroscopy, CRC Press*, 2009.
[14] M. Haltmeier, O. Scherzer, P. Burgholzer, and G. Paltauf. Thermoacoustic computed tomography with large planar receivers. *Inverse Problems*, 20(5):1663–1673, 2004.

[15] M. Haltmeier, T. Schuster, and O. Scherzer. Filtered backprojection for thermoacoustic computed tomography in spherical geometry. *Math. Methods Appl. Sci.*, 28(16):1919–1937, 2005.
[16] Y. Hristova. Time reversal in thermoacoustic tomography – an error estimate. *Inverse Problems*, 25(5):055008, 2009.
[17] Y. Hristova, P. Kuchment, and L. Nguyen. Reconstruction and time reversal in thermoacoustic tomography in acoustically homogeneous and inhomogeneous media. *Inverse Problems*, 24:055006, 2008.
[18] X. Jin and L. V. Wang. Thermoacoustic tomography with correction for acoustic speed variations. *Phys. Med. Biol.*, 51:6437–6448, 2006.
[19] R. A. Kruger, W. L. Kiser, D. R. Reinecke, and G. A. Kruger. Thermoacoustic computed tomography using a conventional linear transducer array. *Med Phys*, 30(5):856–860, May 2003.
[20] R. A. Kruger, D. R. Reinecke, and G. A. Kruger. Thermoacoustic computed tomography–technical considerations. *Med Phys*, 26(9):1832–1837, Sep 1999.
[21] G. Ku, B. Fornage, X. Jin, M. Xu, K. Hunt, and L. V. Wang. Thermoacoustic and photoacoustic tomography of thick biological tissues toward breast imaging. *Tech. Cancer Research and Treatment*, 4:559–565, 2005.
[22] P. Kuchment and L. Kunyansky. Mathematics of thermoacoustic tomography. *European J. Appl. Math.*, 19(2):191–224, 2008.
[23] S. K. Patch. Thermoacoustic tomography – consistency conditions and the partial scan problem. *Physics in Medicine and Biology*, 49(11):2305–2315, 2004.
[24] J. Qian, P. Stefanov, G. Uhlmann, and H. Zhao. An efficient neumann series-based algorithm for thermoacoustic and photoacoustic tomography with variable sound speed. *SIAM J. Imag. Sci.*, 4:850–883, 2011.
[25] P. Stefanov and G. Uhlmann. Thermoacoustic tomography with variable sound speed. *Inverse Problems*, 25(7):075011, 16, 2009.
[26] P. Stefanov and G. Uhlmann. Thermoacoustic tomography arising in brain imaging. *Inverse Problems*, 27:045004, 2011.
[27] L. V. Wang and H.-I. Wu. *Biomedical Optics: Principles and Imaging*. Wiley-Interscience, New Jersey, 2007.
[28] M. Xu and L.-H. V. Wang. Universal back-projection algorithm for photoacoustic computed tomography. *Phys. Rev. E.*, 71:016706, 2005.
[29] M. Xu and L. V. Wang. Photoacoustic imaging in biomedicine. *Review of Scientific Instruments*, 77(4):041101, 2006.
[30] Y. Xu and L. V. Wang. Effects of acoustic heterogeneity in breast thermoacoustic tomography. *IEEE Trans. Ultra. Ferro. and Freq. Cont.*, 50:1134–1146, 2003.
[31] Y. Xu and L. V. Wang. Rhesus monkey brain imaging through intact skull with thermoacoustic tomography. *IEEE Trans. Ultrason., Ferroelectr., Freq. Control*, 53(3):542–548, 2006.
[32] X. Yang and L. V. Wang. Monkey brain cortex imaging by photoacoustic tomography. *J Biomed Opt*, 13(4):044009, 2008.

Department of Mathematics, The Chinese University of Hong Kong, Hong Kong SAR
E-mail address: tschung@math.cuhk.edu.hk

Department of Mathematics, The Chinese University of Hong Kong, Hong Kong SAR
E-mail address: cylam@math.cuhk.edu.hk

Department of Mathematics, Michigan State University, 619 Red Cedar Rd RM C306, East Lansing, MI 48824-3429
E-mail address: qian@math.msu.edu